

Experimental and Theoretical Investigation of Corrosion Inhibition Effect of Multi-Active Compounds on Mild Steel in 1 M HCl

Shulei Fu¹, Shengtao Zhang^{1,*}, Qin Xiang¹, Weiya Tan¹, Wenpo Li^{1,*}, Shijin Chen², Lei Guo³

¹ School of Chemistry and Chemical Engineering, Chongqing University, Chongqing 400044, China.

² Bomim Electronics Ltd., Meizhou 514021, China.

³ School of Materials and Chemical Engineering, Tongren University, Tongren 554300, China.

*E-mail: stzhang_cqu@163.com, liwenpo@aliyun.com

Received: 3 March 2019 / Accepted: 24 April 2019 / Published: 10 June 2019

The corrosion resistance of three compounds, namely, thiabendazole (TBD), benzimidazole (BD), and thiazole (TA) on Q235 steel in 1 M HCl medium were investigated with electrochemical experiments, surface analysis and theoretical calculations. The results received by electrochemical experiments are consistent with the surface morphology observation including FE-SEM and AFM, which indicates that the efficiency of TBD is higher than BD and TA. The adsorption of all corrosion inhibitors on the steel surface follows the Langmuir adsorption isotherm. Furthermore, XPS, quantum chemical calculation and molecular dynamics simulations were carried out to interpret inhibition mechanism of these inhibitor compounds for steel.

Keywords: Corrosion inhibitor; HCl; Mild Steel; XPS; Quantum chemical calculation.

1. INTRODUCTION

Mild steel is widely employed for automobile, aviation, construction, chemical industry and other industrial fields because of its excellent properties and affordable price. However, the main problem is that the corrosion resistance of steel is very weak under acidic conditions. Fortunately, adding corrosion inhibitors is the most simple and efficacious method to decrease metal corrosion [1, 2].

Heteroatom organic chemical compounds were studied as corrosion inhibitors for many years. They can adsorb on the metal surface and then create an efficacious protective layer due to the heteroatoms, conjugate double bonds, aromatic rings and so on [3-9]. Previously studied organic compounds cannot be widely used because of their toxicity and high cost. The increasing concern

about the environment makes it necessary to research some efficient, cheap, and low toxic corrosion inhibitors [1, 10]. The structure of organic compounds, the metal surface charge and the type of aggression medium all influence the ability of the studied inhibitors to reduce the metal corrosion [11, 12]. Therefore, the main barrier in designing a new inhibitor is its complicated and unclear inhibition mechanism. As a result, the main way to choose the corrosion inhibitor is still blind selection.

To alleviate the above problem, clarify the structure-efficiency relationship of the inhibitor molecule is very important. In present study, we attempted to obtain new insights into the effects of multi-sites adsorption on the inhibition performance of organic molecule. Thiabendazole (TBD), a systemic fungicide used to treat fruits and vegetables, has low toxic to the environment process [13]. As known, the molecular structure of TBD is a combination of benzimidazole (BD) and thiazole (TA) compound. The objective of this paper was thus to research the inhibition ability of TBD on steel corrosion in 1 M HCl. As a comparison, the inhibition properties of BD and TA were also studied. Specifically, various methods including electrochemical techniques like dynamic potential polarization curves (Tafel) and electrochemical impedance spectroscopy (EIS), specifically surface study like scanning electron microscope (SEM) and atomic force microscope (AFM) have been used to investigate the inhibition behavior of these three compounds. Moreover, quantum chemical calculation, molecules dynamics (MD) simulation and X-ray photoelectron spectroscopy (XPS) were conducted to demonstrate the inhibition mechanism of studied inhibitors at the molecular or atomic level.

2. EXPERIMENTAL

2.1 Materials preparation

Three corrosion inhibitors, benzimidazole (BD), thiazole (TA) and thiabendazole (TBD) in this study is shown in Fig. 1. Q235 steel specimen with the quality score composition of 0.05% P, 0.12% Mn, 0.17% Si, 0.05% P, 0.20% C and balance Fe was researched for the tests. The size of steel specimens was 0.5 cm × 0.5 cm × 0.5 cm for scanning electron microscope, 0.1 cm × 1 cm × 1 cm for atomic force microscope and 1 cm² exposed area for electrochemical tests. Prior to each measurement, all samples should be sanded with a series of sandpapers, then ultrasonic cleaned by absolute ethanol and distilled water, and finally dried in cold air. All of the tests were performed in 1 M HCl before and after adding the corrosion inhibitors.

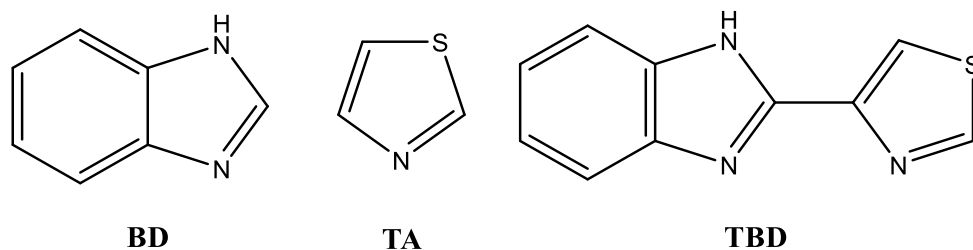


Figure 1. The molecular structures of studied inhibitors.

2.2 Electrochemical tests

The experimentations of electrochemical were implemented by a three-electrode system with CHI 660E working station. Saturated calomel electrode, tested steel specimen and Pt were adopted as reference electrode, working electrode and counter electrode, respectively. The test temperature is constant at 298 ± 1 K. A stabilized open circuit potential (E_{OCP}) was first obtained after 0.5 h immersion in the test medium. Electrochemical impedance spectra (EIS) measurement was tested at the last stable E_{OCP} , the frequency range were set as 100000-0.01Hz and the perturbation amplitude is 10 mV peak-to-peak. Obtained EIS results have been further fitting with ZsimpWin 3.10 software. Eventually, a potentiodynamic scanning method with a scan rate of 1 mV s^{-1} is used to the polarization curve test. In order to ensure the accuracy and reproducibility of the experiment, each measurement was carried out for 3 times under the same experimental conditions.

2.3 Surface characterization

The steel samples were investigated by AFM (Asylum Research) and FE-SEM (JEOL-JSM-7800F, JEOL Ltd) under the condition of immersion in 1 M HCl with or without those inhibitors to watch the surface appearance. XPS (ESCALAB 250Xi, Thermo Scientific) was applied to investigate the elements composition of TBD and binding information on steel surface.

2.4 Computational methods

Quantum chemical calculation of the three inhibitors were proceed with Materials Studio software. The geometric structure of these molecules was researched by density functional theory (DFT). The consequence parameters including E_{HOMO} , E_{LUMO} , $\Delta E = E_{\text{LUMO}} - E_{\text{HOMO}}$ and μ .

The adsorption conduct of three chemical compounds on steel surface was researched by using MD simulation. The densely packed Fe (110) was selected as tested surface because of the low Miller index iron surface [14]. In the MD simulation, the simulation time was 500 ps with the time pace of 1 fs in 298 K.

3. RESULTS AND ANALYSIS

3.1 Potentiodynamic polarization

Tafel curves of mild steel in the presence and absence of different concentrations of BD, TA and TBD in 1 M HCl at 298 K was illustrated in Fig. 2. The relevant parameters like I_{corr} (corrosion current density), E_{corr} (corrosion potential), β_a , β_c (cathodic and anodic Tafel inclines) and η (inhibition efficiency) were listed in Table 1.

In the case, the inhibition efficiency was estimated according to coming after equation:

$$\eta = \frac{I_{corr,0} - I_{corr}}{I_{corr,0}} \times 100 \tag{1}$$

where $I_{corr,0}$ stands for the uninhibited current densities and I_{corr} represents the inhibited of mild steel specimens.

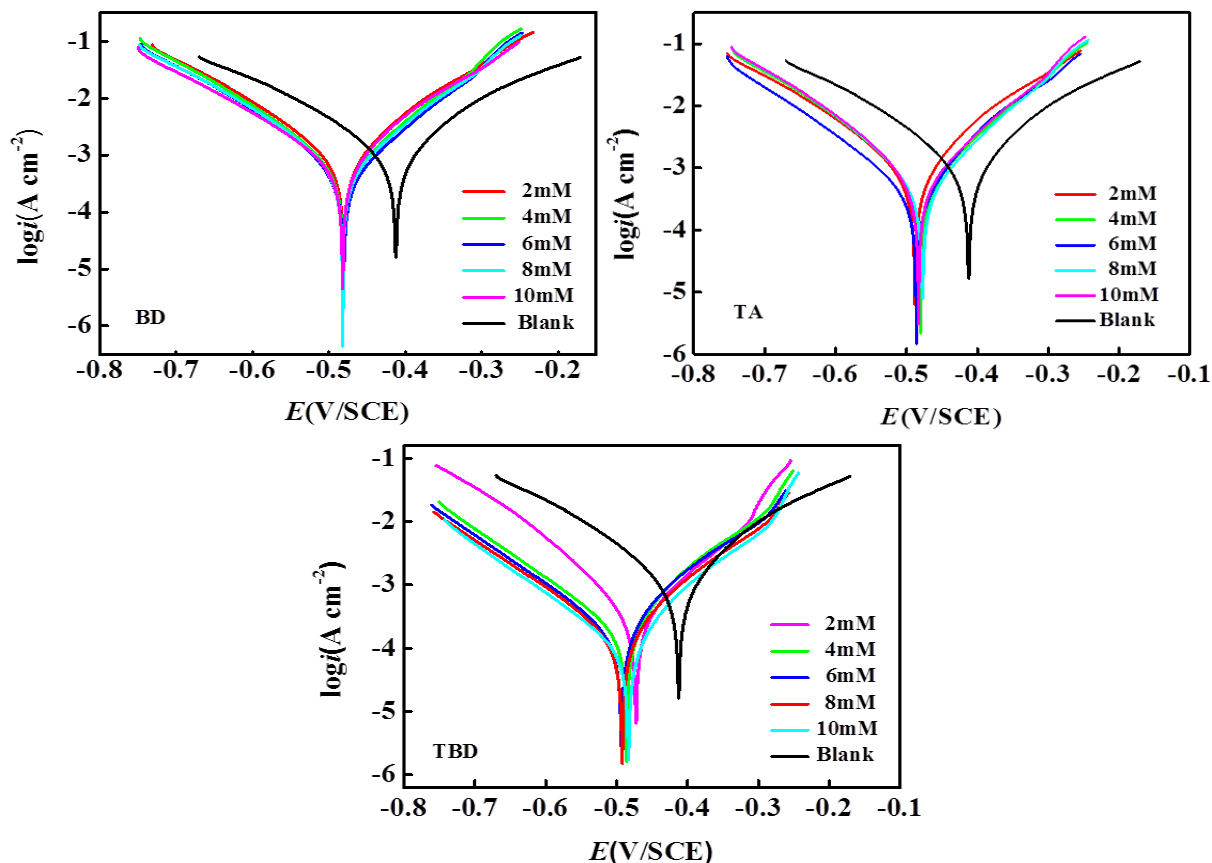


Figure 2. Polarization curves of mild steel with different concentrations of BD, TA and TBD in 1 M HCl.

As demonstrated in Fig. 2, the corrosion current densities of all anodic and cathodic plots for BD and TA decreased insignificantly, which indicates that the protection for steel corrosion is not favorable for the two inhibitors in the medium. As a comparison, both the anodic and cathodic curves moving toward to the low prevailing densities obviously with the augment of the concentrations of TBD, and at the same time the η increases, demonstrating that the addition of TBD can significantly inhibit metal corrosion [15-17]. Particularly, it is clear that all polarization curves are almost parallel to each other, revealing that these corrosion inhibitors did not change the mechanism of steel dissolution and hydrogen reduction. As a result, the activation-controlled hydrogen evolution and the inhibitor molecules shows geometric retardation effect [18-21].

Table 1. The polarization parameters for mild steel in the absence and presence of varying concentrations of BD, TA and TBD in 1 M HCl.

<i>C</i> (mM)	E_{corr} (V)	I_{corr} (mA cm ²)	β_a (mV dec ⁻¹)	β_c (mV dec ⁻¹)	η (%)
Blank	-0.441	0.955	84.3	85.2	–
BD					
2	-0.482	0.805	107	142	16
4	-0.481	0.607	103	115	37
6	-0.481	0.497	105	115	48
8	-0.482	0.711	105	141	26
10	-0.482	0.757	114	138	21
TA					
2	-0.488	0.713	103	134	25
4	-0.480	0.581	109	122	39
6	-0.486	0.429	101	137	55
8	-0.487	0.408	86	90.	57
10	-0.483	0.593	104	109	38
TBD					
2	-0.473	0.314	108	98	67
4	-0.486	0.199	84	127	79
6	-0.493	0.184	93	131	81
8	-0.492	0.148	99	128	85
10	-0.475	0.056	87	126	94

As it illustrated in Table 1, the corrosion potential shifts toward more negative potential, the largest displacement of E_{corr} for BD, TA and TBD are 41 mV, 47 mV and 52 mV, respectively. When the fluctuation of E_{corr} is under 85 mV, the type of this inhibitor is mixed [22]. Therefore, all these three inhibitors are mixed-type inhibitors. For BD and TA, with the concentration rises, the inhibition efficiency increases first and then decreases. The maximum values of η are 48% for BD at the concentration of 6 mM and 57% for TA at the concentration of 8 mM, respectively. However, for TBD, the inhibition efficiency increased as the concentration increased, reaching a maximum value of 94% at 10 mM.

3.2 Electrochemical impedance spectroscopy

To clearly understand surface properties of the steel, EIS researches for steel in 1 M HCl with inhibitors or not were carried out. The Nyquist and Bode graphs are painted in Figs. 3 and 4, respectively.

As it is shown in Fig. 3, a single of capacitive loop appears in the Nyquist plots, it is ordinarily due to charge transfer resistance [14]. After adding these corrosion inhibitors, the shape of the Nyquist diagrams did not change significantly, indicating that these inhibitors have little effect on the corrosion mechanism of the steel in 1 M HCl. For BD and TA, the diameter of the capacitive arcs increases first and then decreases with the increasing concentration of corrosion inhibitors. The optimum

concentration for BD and TA is 6 mM and 8 mM, respectively. This reveals that over concentration will cause irregular arrange of organic molecules, which reduces the corrosion inhibitive ability [23]. Compared to the blank experiment, the radius of the semicircles increases non-significantly after adding BD and TA. However, the diameter of the Nyquist curves increases dramatically with addition of TBD, indicating that a dense protective layer is gradually created on the steel surface and brings about a better protective effect.

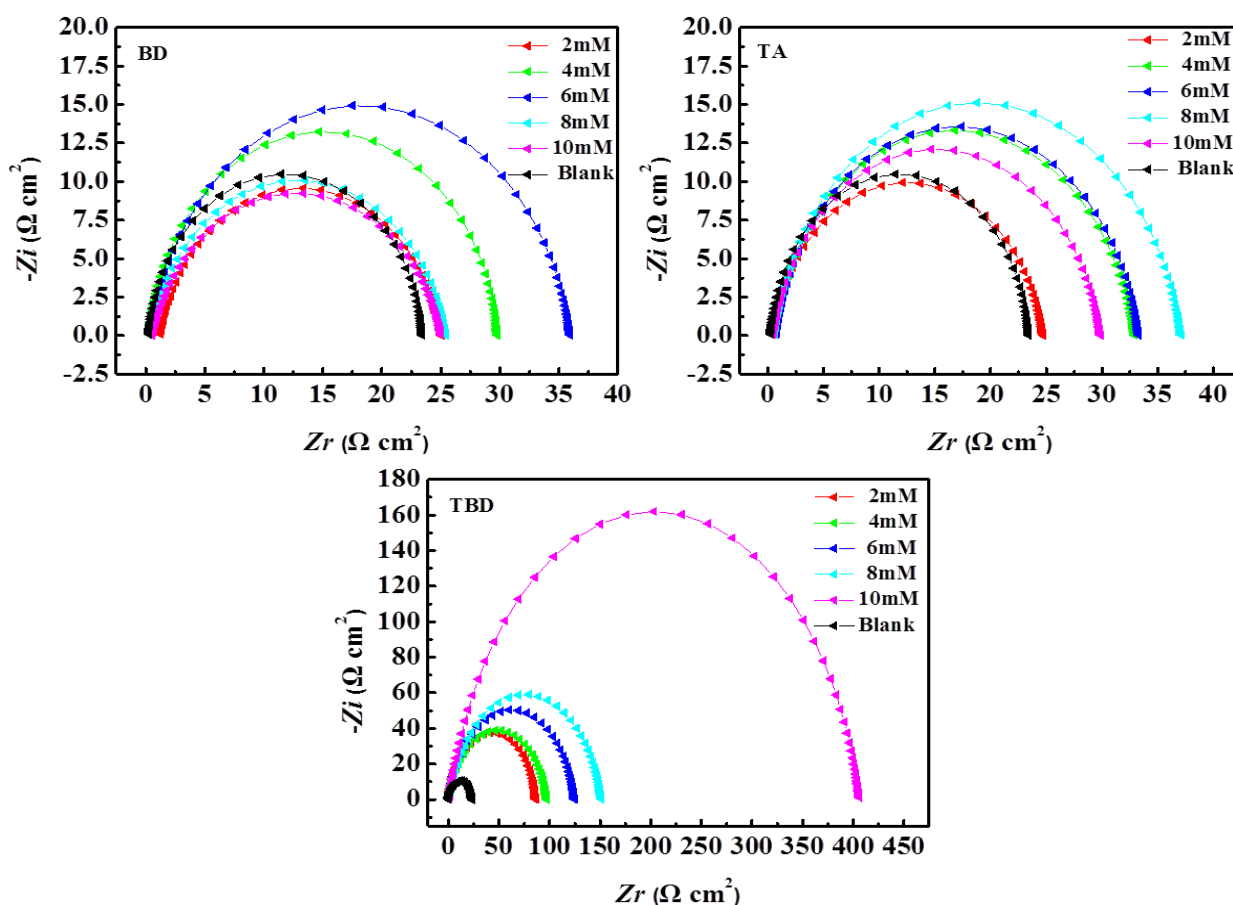


Figure 3. Nyquist plots of steel without and with various concentrations of BD, TA and TBD in 1 M HCl.

For the Bode patches that are shown in Fig. 4, we can see that the maximum phase angle change is very small for BD and TA in comparison with the blank. But for TBD, one order of magnitude is augmented by the value of the impedance in low-frequency when compared to the blank experimentation, indicating TBD is executed as a high efficiency inhibitor for mild steel in acid solution. With the increasing concentration of the inhibitor, the frequency range with the maximum phase angle turns larger, indicating that TBD can be firmly adsorbed on steel surface.

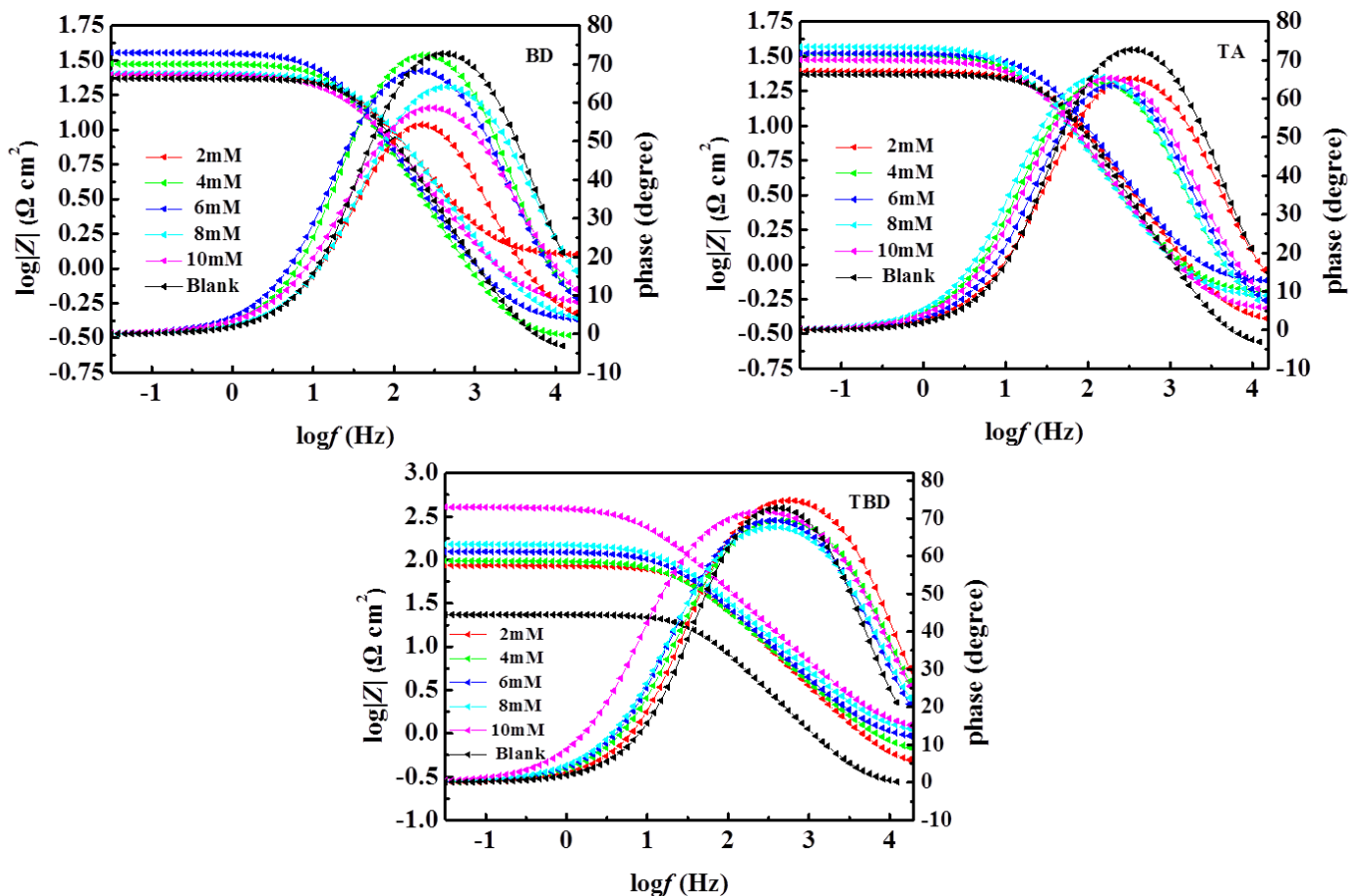


Figure 4. Bode plots of steel with and without various concentrations of BD, TA and TBD in 1 M HCl solution.

So as to further study the mechanism of the three-electrode system after powering up, the corresponding equivalent circuits which shown in Fig. 5 is used [24]. In this figure, the solution resistance is represented by R_s and the charge transfer resistance is represented by R_{ct} . The CPE is constant phase angle element. All these data have been fitted and listed in Table 2.

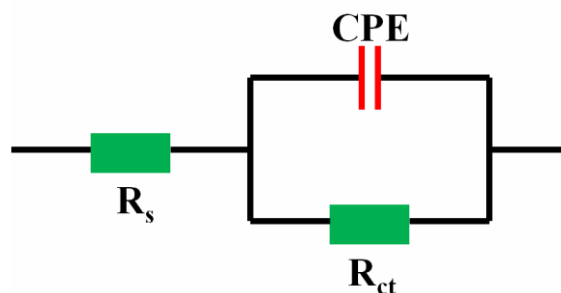


Figure 5. Electrochemical equivalent circuits.

CPE impedance can compute using the following formula [25, 26]:

$$Z_{CPE} = \frac{1}{Y_0(j\omega)^n} \tag{2}$$

where j is imaginary root, ω is angular frequency, Y_0 is magnitude of the CPE , n is deviation parameter which can express the phase shift. $n = 0$, the CPE can be regarded as a pure resistance, $n = 1$, it can be regarded as a pure capacitor [27]. Furthermore, the value of C_{dl} , which can be expressed as below:

$$C_{dl} = \frac{\epsilon^0 \epsilon}{d} S \tag{3}$$

Wherein ϵ^0 , ϵ represents the local dielectric constant of the air and electric double layer, d is double layer thickness and S is used as steel electrode surface area. The corrosion inhibitor replaces the adsorption of water on steel surface, thus causing the electric double layer become thicken, while the local dielectric constant and the metal exposed area become smaller [28]. Both of the factors are leading to the reduce of C_{dl} .

The inhibited efficiency of these inhibitors is computed from R_{ct} by the following formula:

$$\eta = \frac{R_{ct} - R_{ct}^0}{R_{ct}} \times 100 \tag{4}$$

wherein R_{ct} , $R_{ct,0}$ represent the charge transfer resistance for mild steel in the absence of inhibitors and in blank solution.

Table 2 shows that the R_{ct} changes with the increasing concentration of inhibitors, which discloses that the film developed or disappeared on the steel surface. Especially, the increasing trend of R_{ct} values for TBD is more obvious than the other two inhibitors, and the inhibited efficiency show an increasing tendency with the increasing concentrations. But for BD and TA, as the concentration increases, the R_{ct} increase first and then decrease, indicating that over-concentration could destroy the adsorption film [23].

Table 2. Parameters obtained from impedance measurements for steel at varying concentrations of (a)BD, (b)TA and (c)TBD.

C (mM)	R_s ($\Omega \text{ cm}^2$)	R_{ct} ($\Omega \text{ cm}^2$)	CPE		η %
			Y($\mu\text{F cm}^2$)	n	
Blank	0.248	23.17	262.9	0.94	–
BD					
2	1.227	23.82	370.0	0.86	3
4	0.316	29.48	360.2	0.93	21
6	0.414	35.54	442.2	0.89	35
8	0.402	25.03	579.3	0.86	7
10	0.533	24.52	337.1	0.82	6
TA					
2	0.364	24.35	365.2	0.88	5
4	0.616	32.31	490.4	0.88	28
6	0.734	32.56	327.0	0.89	28
8	0.576	36.53	511.4	0.88	36
10	0.460	29.40	477.6	0.88	21
TBD					
2	0.393	86.02	96.9	0.91	73
4	0.547	96.81	137.3	0.86	76
6	0.807	123.8	119.4	0.87	81
8	0.945	150.3	117.5	0.85	85
10	1.007	405.2	83.3	0.86	94

Consequently, inhibition efficiencies reach 35% for BD at 6 mM, 37% for TA at 8 mM and 94% for TBD at 10 mM, respectively. This indicates that TBD can prevent the steel corrosion effectively in acid medium. These consequences from the EIS experimentation are in complete agreement with the outcomes gained in the polarization curves above.

3.3 SEM analysis

Before and after 8 h of immersion in the absence and presence of researched organic compounds at optimum concentration in 1 M HCl, the SEM micrographs of the steel surface are presented in Fig. 6. The images manifest that whether add the inhibitors or not, the steel surface has varying degrees of corrosion. Fig. 6a shows the surface of the steel that was newly polished. It can be seen that the surface is very smooth at this time, with only some shallow scratches. Fig. 6b displays the steel surface was harshly destroyed after immersed in 1 M HCl solution. After immersed in the solution with 6 mM BD, shown in Fig. 6c, the surface of the steel is not much different from the blank. And with addition of 8 mM TA, shown in Fig. 6d, the metal surface still has obvious signs of corrosion. However, the surface of the specimen in Fig. 6e was much less damaged due to the presence of 10 mM TBD, and can be seen that the inhibitor was adsorbed on the metal surface, demonstrating excellent inhibition of TBD. Additionally, it can be concluded that the inhibition ability of TBD is better than TA and BD. The result is coordinates with the electrochemical test data.

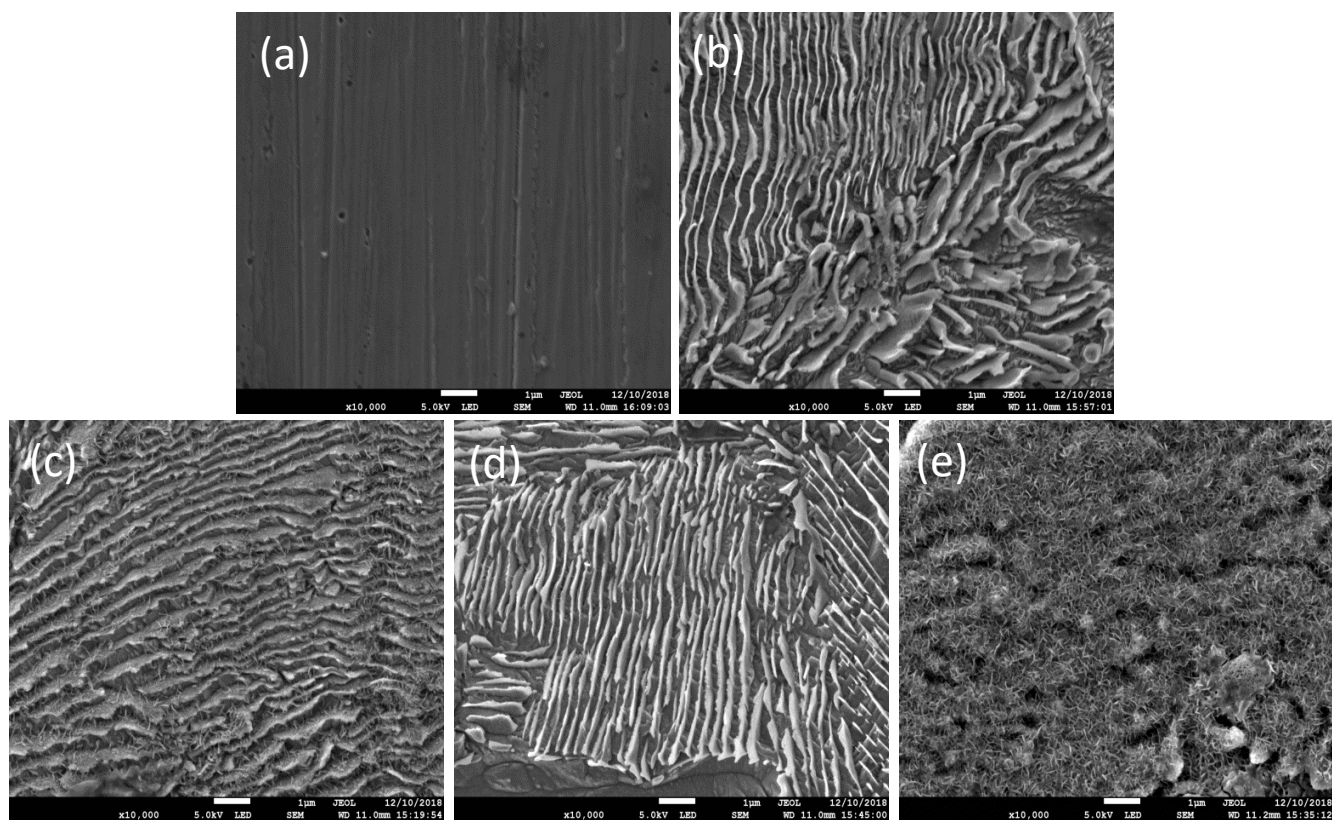


Figure 6. SEM of the mild steel soaked for 8 h in 1M HCl solution in the absence and presence of inhibitors (a) Blank, (b) BD, 6 mM, (c) TA, 8 mM, and (d) TBD, 10 mM.

3.4 AFM analysis

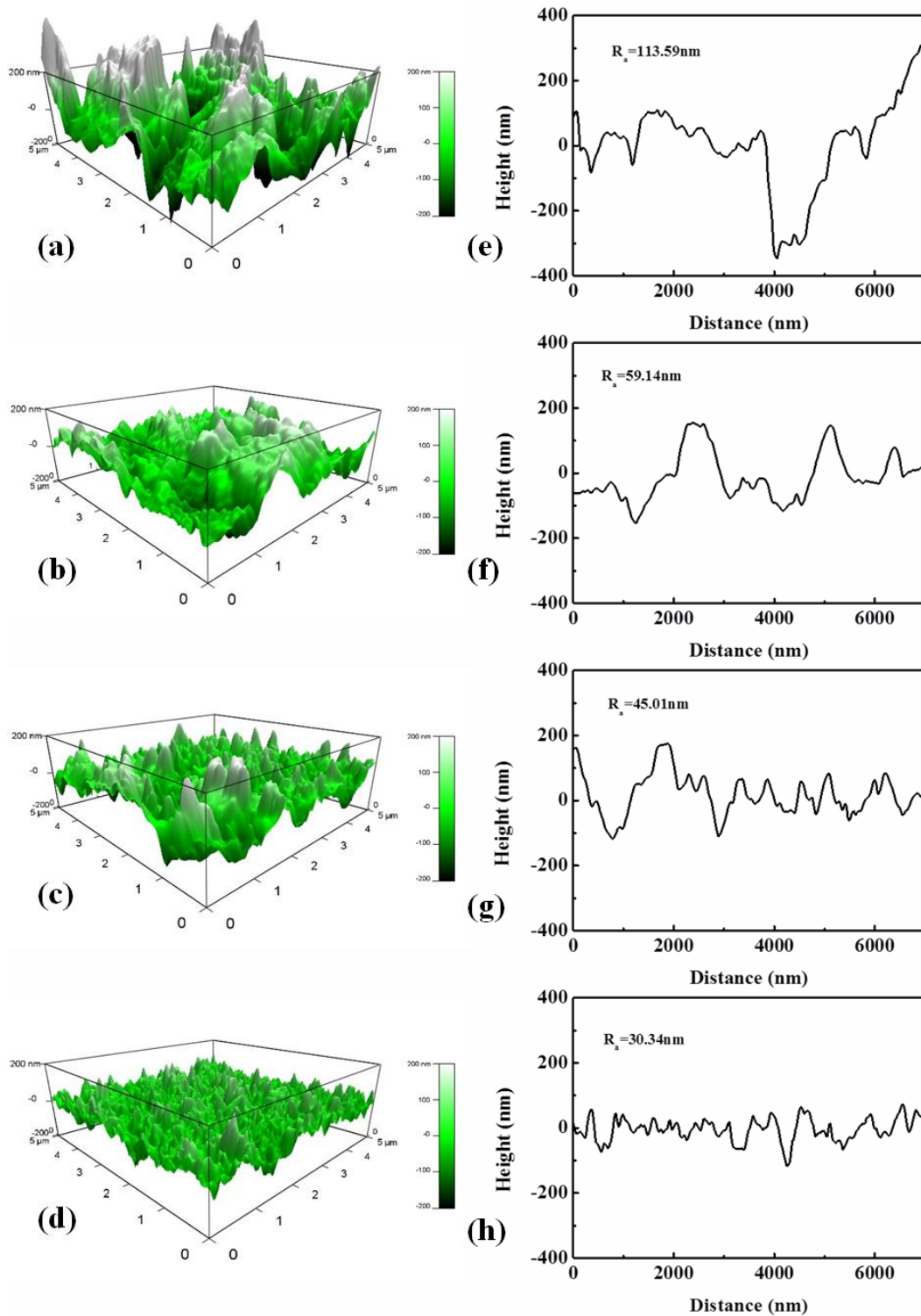


Figure 7. The height profile and AFM graphs of mild steel (a, e) without inhibitors, (b, f) with 6 mM BD, (c, g) with 8 mM TA, and (d, h) with 10 mM TBD in 1 M HCl for immersion 2 h at 298 K.

The 3D AFM graphs and height profiles of steel surface for 2 h immersion in the absence and presence of inhibitors in 1 M HCl at 298 K are expressed in Fig. 7. Clearly, 3D AFM pattern of the specimens exposed to acid solution without inhibitors shows that the steel is extremely damaged and

emerging a configuration like mountain peak and valley with many deep and large holes. However, with addition of TBD, the surface appears smoother and hence less corroded, which pointed out that the steel corrosion rate substantially declines (Fig. 7c, f).

Average roughness obtained from the blank and with the addition of BD, TA, TBD treatment are 113.59 nm, 59.14 nm, 45.01 nm and 30.34 nm, respectively. The maximal peak-to-valley height (P–V) of the uninhibited surface is 919.49 nm and of TBD treated surface is 331.15 nm, which reduced a lot. These data proved that the surface becomes smoother and the corrosion degree decreases due to the adsorption of inhibitors on the steel surface. This finding in a well accord with the consequences received from electrochemical experimentations and SEM test.

3.5 XPS analysis

To go over the adsorption behavior of inhibitors on metal surface, X-ray photoelectron spectroscopy (XPS) examination was took on the steel surface after 2 h soaking in 1 M HCl without and with 10 mM TBD. Fig. 8 compares the blank and TBD in representative XPS survey spectra. And the XPS spectrums, shown in Figs. 9 and 10, were resulted from 1 M HCl solution treated steel surface (O 1s, C 1s, Fe 2p) and 1 M HCl with 10 mM TBD treated steel surface (O 1s, N 1s, C 1s, Fe 2p, S 2p). Each peak corresponding binding energies (BE, eV) and homologous bonds were presented in Table 3.

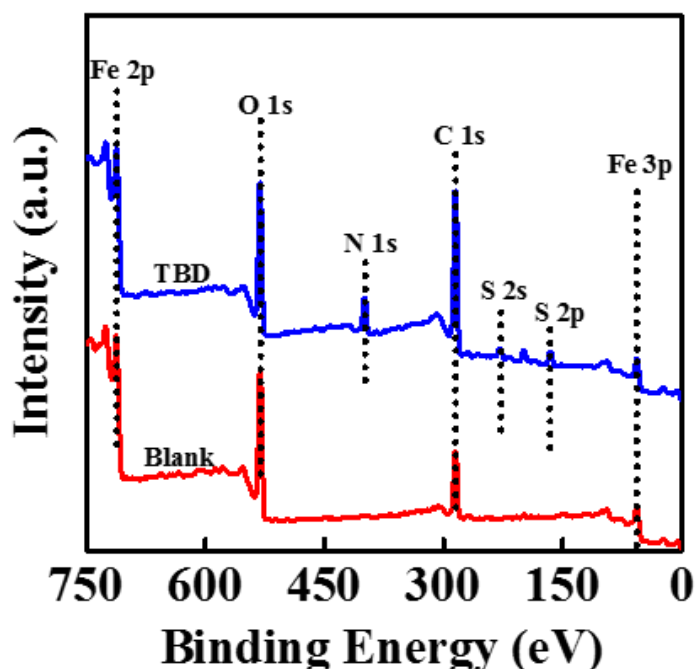


Figure 8. Representative XPS survey spectra from Blank and TBD.

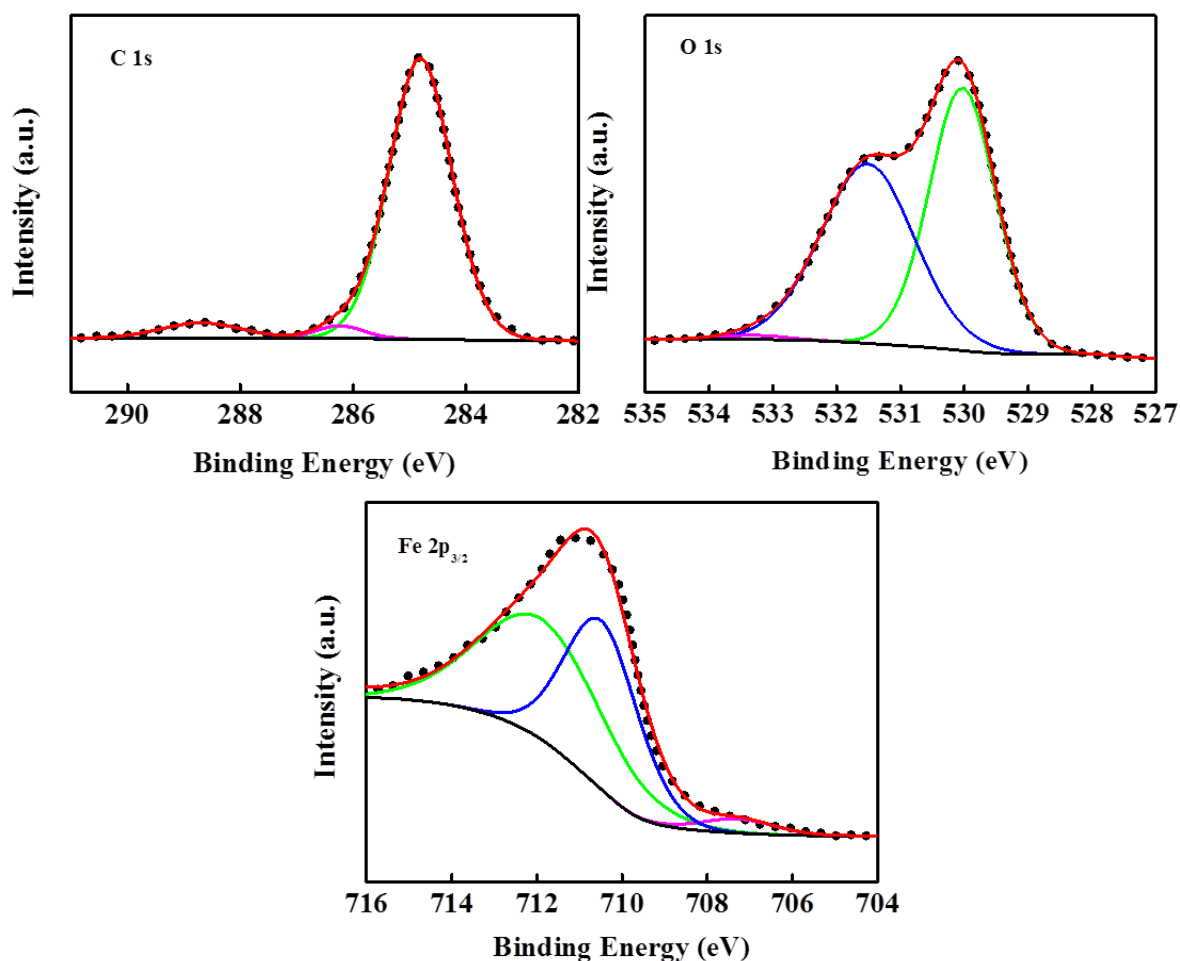


Figure 9. XPS spectroscopy of O 1s, C 1s and Fe 2p for Blank.

Table 3. Binding energy (eV), relative major core lines for the Blank and TBD substrates.

Substrate	C 1s		O 1s		Fe 2p		N 1s		S 2p	
	BE(eV)	Assignment	BE(eV)	Assignment	BE(eV)	Assignment	BE(eV)	Assignment	BE(eV)	Assignment
Blank	284.80	C-C, C-H	530.03	O ²⁻ (Fe ₂ O ₃ , Fe ₃ O ₄)	707.27	Fe ⁰	-	-	-	-
	286.24	C=O	531.51	OH ⁻ (FeOOH)	710.48	Fe ²⁺ , Fe ³⁺ (Fe ₂ O ₃ , Fe ₃ O ₄)	-	-	-	-
	288.69	C ⁺ -O	533.31	Adsorbed H ₂ O	711.88	FeOOH	-	-	-	-
TBD	284.80	C-C, C=C, C-H	530.25	O ²⁻ (Fe ₂ O ₃ , Fe ₃ O ₄)	709.70	Fe ²⁺ , Fe ³⁺ (Fe ₂ O ₃ , Fe ₃ O ₄)	398.59	N-C	164.85	S-C
	286.04	C-N, C=N, C-S	531.77	OH ⁻ (FeOOH)	711.00	FeOOH	399.59	=N-	165.98	S-Fe
	288.61	C-N ⁺	533.63	Adsorbed H ₂ O	713.54	Fe(III)	400.29	=N-Fe	-	-

As shown in Fig. 8, the XPS survey spectra shows all the elements on the metal surface for blank and TBD. Both of them contain elements as follows: Fe 2p, O 1s and C 1s. The difference is that the N 1s and S 2p is only detected in TBD, it illustrates that on the steel surface the TBD molecular is sure to be detected.

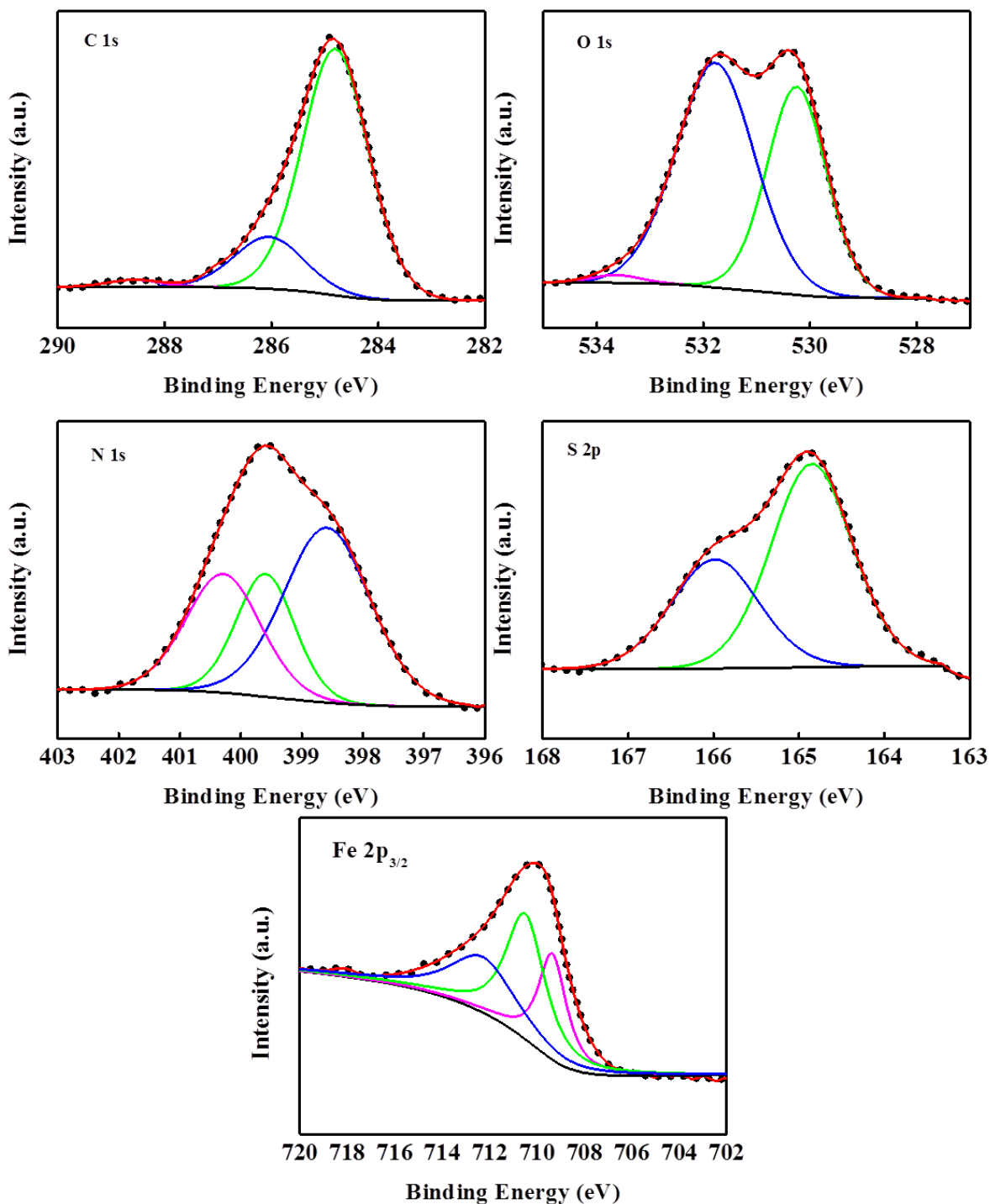


Figure 10. XPS spectroscopy of O 1s, N 1s, C 1s, Fe 2p and S 2p for TBD.

The deconvoluted C 1s spectrum from Blank is shown in Fig. 9, it can be divided into three peaks. The first and main peak located at 284.8 eV is attributed to C–C and C–H bonds in the contaminant hydrocarbons [29]. The two small peaks at 286.24 eV and 288.69 eV can be in line with the C⁺–O and C=O bonds [30]. As shown in Fig. 10, the C 1s spectrum from TBD treated metal surface also presents three peaks. The largest peak that is located at 284.8 eV is associated with the

aromatic bonds [15]. The one at 286.04 eV is connected to the C–N, C=N of imidazole and the C–S of thiazole ring. The last component at 288.61 eV possibly ascribed to C–N⁺ which due to protonation of =N– in the imidazole [26].

The O 1s spectra for both Blank and TBD specimens are also divided into three peaks. Located at 530.03 eV (Blank) and 530.25 eV (TBD) is the first peak correspond to O²⁻, it could be owing to the oxygen atoms from Fe₂O₃ and/or Fe₃O₄ [31]. The peak located at 531.51 eV (Blank) and 531.77 eV (TBD) is usually ascribable to OH⁻ from FeOOH which indicates hydrous iron oxides [32]. The last component at 533.31 eV (Blank) and 533.63 eV (TBD) is connected to O of the adsorbed water [33].

A double peak profile that is located at 711 eV (Fe 2p_{3/2}) and 725 eV (Fe 2p_{1/2}) is depicted by The Fe 2p part spectra for steel surface [30]. Fig. 9 shows the Fe 2p_{3/2} spectrum for Blank specimen which is divided into three peaks. Peak at 707.27 eV is due to metallic iron [34]. And the last two peaks located at 710.48 eV and 711.88 eV is associated to ferric oxide like Fe₂O₃/Fe₃O₄ [34] and hydroxide species like FeOOH [35]. For TBD treated steel in Fig. 10, the Fe 2p_{3/2} spectra is depicted into three peaks. Compared to the Blank, the peak for metallic iron is disappeared, this may due to the adsorption of inhibitor that covering the substrate. The first two peaks at 709.7 eV and 711 eV is also attributed to ferric oxide like Fe₂O₃/Fe₃O₄ and hydroxide species like FeOOH as the same as Blank. The last peak at 713.54 eV is associated to satellite of Fe(III) [36].

And for N 1s detected only in TBD specimen is shown in Fig. 10, it is divided into three peaks. The first component is the largest contribution at 398.59 eV possibly ascribed to N–C bonds in the imidazole ring [32]. And the peak at 399.59 eV is responsible to =N– structure also in Imidazole ring [26]. The last component at 400.29 eV is associated with =N–Fe [26] because of the lonely electron pairs on N atom combine with the empty orbit of Fe.

The S 2p spectrum from the TBD treated steel surface can be analyzed with spin-orbit-split doublets which are S 2p_{1/2} and S 2p_{3/2} [26]. The S 2p_{3/2} is situated in 164.85 eV and the S 2p_{1/2} at 165.98 eV. For the part of S 2p_{3/2}, it can be fitting to one peak which presents the S–C bond [37] in TBD molecule. The S 2p_{1/2} is also depicts one single peak associated with S–Fe bond. The result indicates that the TBD adsorbed on steel surface to produce a dense protection layer to inhibit the metal corrosion.

3.6 Adsorption isotherms

For the purpose of further learning the adsorption behavior of the inhibitors on steel surface. Adsorption models usually used as follows: Frumkin, Temkin, Flory-Huggins, El-Awady, Langmuir, Freundlich, and so on [38]. The relevant Langmuir adsorption isotherm can be expressed below,

$$\frac{\theta}{1-\theta} = k_{ads} \cdot C \quad (5)$$

Fig. 11 indicated that the Langmuir adsorption isotherm can be well fitted to the experimental results, indicating that TBD adsorbs on steel surface abide by the Langmuir adsorption isotherm. Table 4 shows the corresponding adsorption thermodynamics parameters [39, 40]. When the ΔG^0_{ads} values is from –40 kJ/mol to –20 kJ/mol, then adsorption process is the result of a combination of physical

adsorption and chemistry adsorption [19, 41]. For TBD, the value of ΔG_{ads}^0 is in the interval of -40 kJ/mol to -20 kJ/mol, then the adsorption type of TBD on the steel surface undergo both physical adsorption and chemistry adsorption.

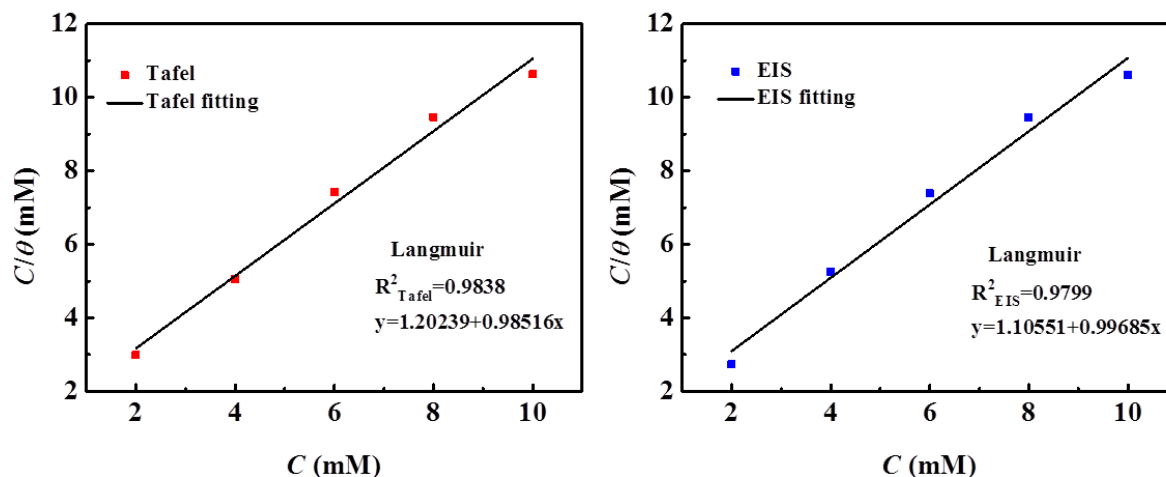


Figure 11. Langmuir adsorption models fitting of TBD on mild steel surface.

Table 4. Corresponding thermodynamic parameters from mild steel.

Measurements	$K_{\text{ads}} (\times 10^3 \text{ L/mol})$	$\Delta G_{\text{ads}}^0 (\text{kJ/mol})$
Tafel	0.83	-26.6
EIS	0.90	-26.8

3.7 Quantum chemical calculation

The quantum chemical calculation test is to study the intrinsic relationship between the structure of corrosion inhibitor and its inhibition ability from the molecular structure. Fig. 12 express the optimized geometrical structure and frontline orbital density distribution of inhibitors. And Table 5 present the corresponding parameters such as E_{LUMO} , E_{HOMO} , ΔE and μ .

In the Fig. 12, LUMO and HOMO orbitals are evenly distributed throughout the molecule of all inhibitors, which indicates that the active sites are distributed over the entire molecule. And from Fig. 12, we can also see that the molecules of these inhibitors are all plane conjugated structure, thereby they can adsorbing on steel surface in a parallel way to get the largest region protecting surface from the attack of the acid solution [42].

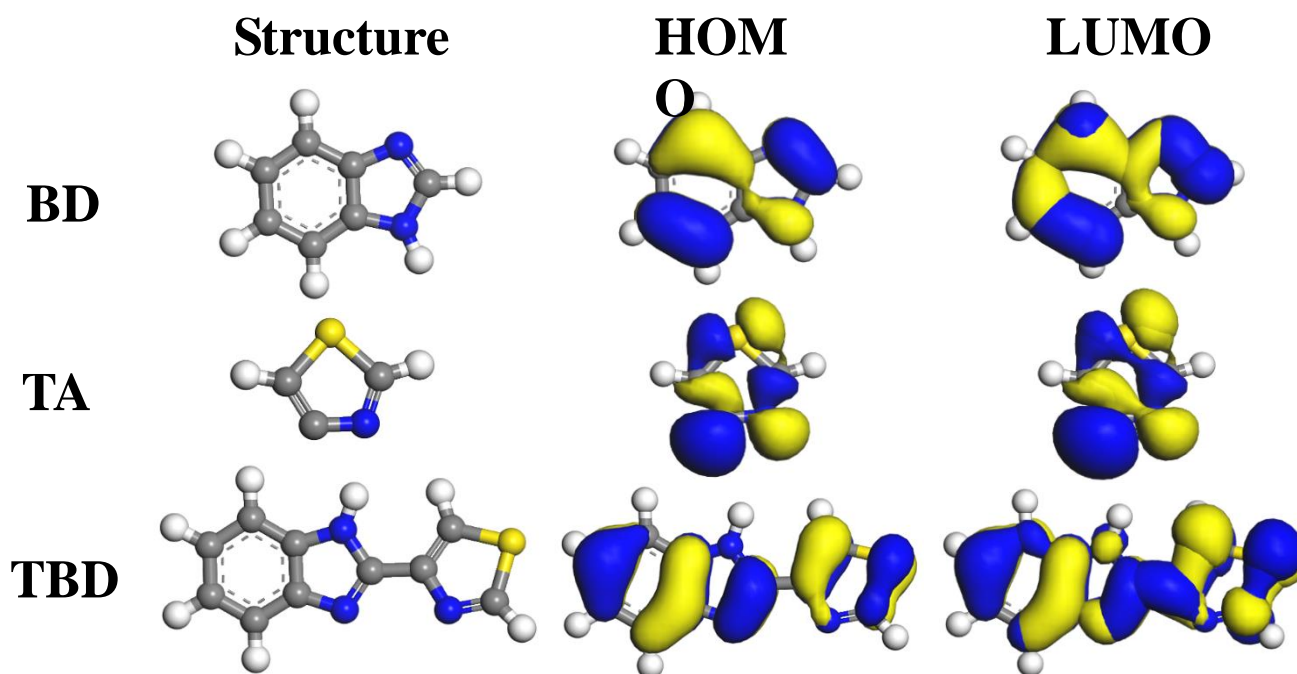


Figure 12. HOMO-LUMO and molecular structure of three studied inhibitors.

Table 5. Corresponding parameters of BD, TA and TBD from quantum chemical calculation.

Compounds	HOMO(eV)	LUMO(eV)	ΔE (eV)	Dipole/debye
BD	-5.5826	-1.3729	4.2097	3.4809
TA	-7.1304	-3.2094	3.9210	2.1587
TBD	-5.4540	-2.3308	3.1232	4.5315

Pursuant to frontier molecular orbital theory, electronic supply ability of molecules influenced the HOMO and the higher value of E_{HOMO} the stronger electron donating ability of inhibitors [10, 43]. Besides, LUMO related to the electron withdrawing ability of molecules and when the E_{LUMO} is more less, the electron absorption ability will be weaker. As is well known, low energy gap (ΔE) value and high dipole moment (μ) value are also represent the higher inhibition efficiency of inhibitors [6, 44]. Furthermore, a lower ΔE value also means that the corrosion inhibitors can easily adsorb on steel surface. And the ΔE values of TBD is lower than BD and TA and the dipole moment (μ) values of TBD is also higher than BD and TA. Therefore, the inhibition ability of TBD is better than BD and TA, this conclusion is in well accordance with the previous one.

3.8 Molecular dynamics simulations

Molecular dynamics simulation was implemented to get further understand of the connection between three investigated inhibitors and steel substrates. The equilibrium adsorption configuration of three corrosion inhibitors on Fe (1 1 0) crystal plane are shown in Fig. 13.

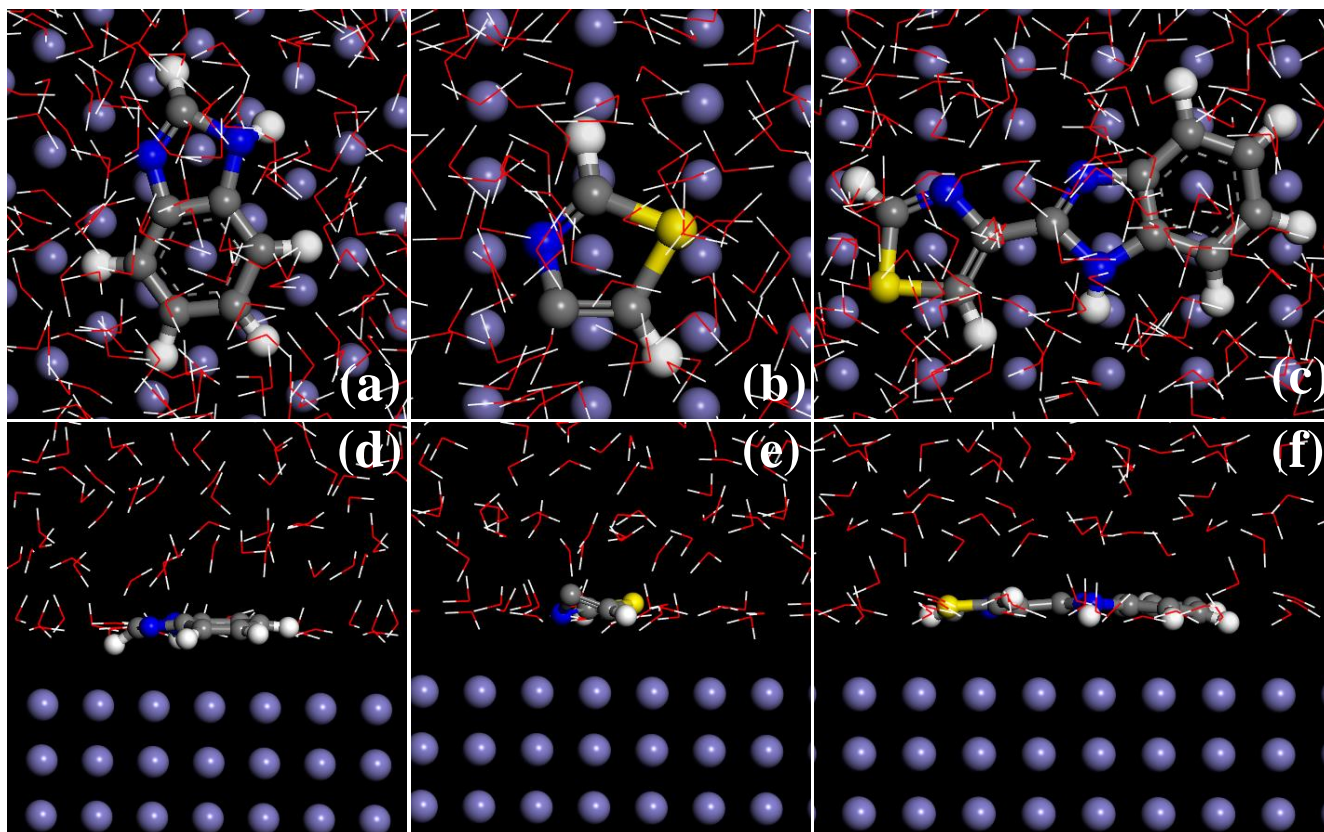


Figure 13. Top and side views of (a)BD, (b)TA and (c)TBD adsorb on Fe(1 1 0) surface.

According to the figure, these three inhibitors are adsorbed on steel surface in a parallel mode. The π -electrons in the corrosion inhibitor molecules can therefore combine with the vacant d-orbital of metallic iron to form a coordination bond [12]. Moreover, the interaction energy (E_{interact}) is calculated as follows [42, 45, 46]:

$$E_{\text{interact}} = E_{\text{tot}} - (E_{\text{subs}} + E_{\text{inh}}) \quad (6)$$

wherein E_{tot} stands for the system total energy, E_{subs} represents the energy of water molecules together with mild steel substrate, E_{inh} stands for the inhibitor energy. The calculated E_{interact} (gained from the above equation) is -535.45 kJ/mol for TBD, -349.39 kJ/mol for BD and -169.36 kJ/mol, respectively. The higher the value of E_{interact} , the better the corrosion inhibition performance of the corrosion inhibitors. This outcome is also in beneficial accordance with the former results.

4. CONCLUSION

Theoretical and experimental results were obtained to prove the following conclusions:

(1) From the electrochemical experiments, all corrosion inhibitors have been proven to be mixed-type. In addition, the addition of TBD forms a dense film on the metal surface to insulate metal from water contact. The maximum inhibition efficiency for TBD is 94.3% (EIS test) at 10 mM, it is much larger than the inhibition efficiency of BD and TA.

(2) From the SEM and AFM studies, compared with BD and TA, TBD makes the metal surface smoother, so the corrosion inhibition effect of TBD is better than that of BD and TA. Moreover, the adsorption study proves the adsorption of TBD on steel surface conforms to Langmuir adsorption model and include both physisorption and chemisorption.

(3) From the theoretical calculation and XPS studies, we can draw a further conclusion that the higher inhibition ability of TBD is attributed to the active sites in TBD molecule is more than BD and TA, which makes the formation of more stable protective film of TBD than BD and TA.

(4) It is confirmed that multi-active sites can increase the corrosion inhibition performance of organic compounds. From the results of quantum chemical calculation, the HOMO and LUMO distributions of the two excellent corrosion inhibitors also confirmed the excellent corrosion inhibition performance of the multi-sites adsorption corrosion inhibitors.

ACKNOWLEDGMENTS

This research was supported by National Natural Science Foundation of China (No. 21676035, 21706195), Sail Plan of Guangdong, China (No. 2015YT02D025).

References

1. Y. Qiang, S. Zhang, B. Tan, S. Chen, *Corros. Sci.*, 133 (2018) 6–16.
2. B. Tan, S. Zhang, H. Liu, Y. Guo, Y. Qiang, W. Li, L. Guo, C. Xu, S. Chen, *J. Colloid Interface Sci.*, 538 (2018) 519–529.
3. M.B.P. Mihajlovic, M.B. Radovanovic, Z.Z. Tasic, M.M. Antonijevic, *J. Mol. Liq.*, 225 (2017) 127–136.
4. H. Lgaz, R. Salghi, K. Subrahmanya Bhat, A. Chaouiki, Shubhalaxmi, S. Jodeh, *J. Mol. Liq.*, 244 (2017) 154–168.
5. Y.J. Qiang, S.T. Zhang, S.Y. Xu, L.L. Yin, *RSC Adv*, 5 (2015) 63866–63873.
6. Y. Qiang, S. Zhang, S. Xu, W. Li, *J. Colloid Interface Sci.*, 472 (2016) 52–59.
7. Y. Qiang, S. Zhang, L. Guo, S. Xu, L. Feng, I.B. Obot, S. Chen, *J. Clean. Prod.*, 152 (2017) 17–25.
8. Zohreh Salarvanda, Mehdi Amirnasr, Milad Talebian, Keyvan Raeissi, S. Meghdadi, *Corros. Sci.*, 114 (2017) 133–145.
9. B. Tan, S. Zhang, Y. Qiang, L. Guo, L. Feng, C. Liao, Y. Xu, S. Chen, *J. Colloid Interface Sci.*, 526 (2018) 268–280.
10. Yujie Qiang, Shengtao Zhang, Lei Guo, Xingwen Zheng, Bin Xiang, S. Chen, *Corros. Sci.*, 119 (2017) 68–78.
11. Djamel Daouda, Tahar Douadi, Hanane Hamani, Salah Chafaa, M. Al-Noaimi, *Corros. Sci.*, 94 (2015) 21–37.
12. Y. Qiang, L. Guo, S. Zhang, W. Li, S. Yu, J. Tan, *Sci. Rep.*, 6 (2016) 33305.
13. J. Feng, Y. Hu, E. Grant, X. Lu, *Food Chem.*, 239 (2018) 816–822.
14. Bochuan Tan, Shengtao Zhang, Yujie Qiang, LiFeng, Chaohui Liao, Yue Xu, S. Chen, *J. Mol. Liq.*, 248 (2017) 902–910.
15. Weiwei Zhang, RuiMa, Huanhuan Liu, Yu Liu, Shuai Li, L. Niu, *J. Mol. Liq.*, 222 (2016) 671–679.
16. Y.W. Liu, Y. Chen, X.H. Chen, Z.N. Yang, Y.Xie, Z. Zhang, *J. Alloys Compd.*, 758 (2018) 184e193.
17. K.F. Khaled, *Electrochim. Acta*, 55 (2010) 6523–6532.
18. Hanane Hamani, Tahar Douadi, Mousa Al-Noaimi, Saifi Issaadi, Djamel Daoud, S. Chafaa, *Corros. Sci.*, 88 (2014) 234–245.

19. Zhihua Tao, Shengtao Zhang, Weihua Li, B. Hou, *Corros. Sci.*, 51 (2009) 2588–2595.
20. Hassane Lgaz, Rachid Salghi, *J. Mol. Liq.*, 225 (2017) 271–280.
21. Ayşe Ongun Yüce, Esra Telli, Başak Doğru Mert, Gülfeza Kardaş, Birgül Yazıcı, *J. Mol. Liq.*, 218 (2016) 384–392.
22. A. Singh, K.R. Ansari, M.A. Quraishi, H. Lgaz, Y. Lin, *J. Alloys Compd.*, 762 (2018) 347–362.
23. Yujie Qiang, Shulei Fu, Shengtao Zhang, Shijin Chen, X. Zou, *Corros. Sci.*, 140 (2018) 111–121.
24. Mohamed El Faydy, Mouhssin Galai, Mohamed Ebn Touhami, Ime Bassey Obot, Brahim Lakhrissi, A. Zarrouk, *J. Mol. Liq.* 248 (2017) 1014–1027.
25. L.L. Liao, S. Mo, H.Q. Luo, N.B. Li, *J. Colloid Interface Sci.*, 499 (2017) 110–119.
26. M. Tourabi, K. Nohair, M. Traisnel, C. Jama, F. Bentiss, *Corros. Sci.*, 75 (2013) 123–133.
27. Qing Qu, Shunling Li, Lei Li, Limei Zuo, Xin Ran, Yao Qu, B. Zhu, *Corros. Sci.*, 118 (2017) 12–23.
28. Song Hong, Wen Chen, Hong Qun Luo, N.B. Li, *Corros. Sci.*, 57 (2012) 270–278.
29. Tianbin Gu, Zhengjun Chen, Xiaohui Jiang, Limei Zhou, Yunwen Liao, Ming Duan, Hu Wang, Q. Pu, *Corros. Sci.*, 90 (2015) 118–132.
30. A. Zarrouk, B. Hammouti, T. Lakhliifi, M. Traisnel, H. Vezin, F. Bentiss, *Corros. Sci.*, 90 (2015) 572–584.
31. H. Zarrok, A. Zarrouk, B. Hammouti, R. Salghi, C. Jama, F. Bentiss, *Corros. Sci.*, 64 (2012) 243–252.
32. F.Z. Bouanis, F. Bentiss, S. Bellayer, J.B. Vogt, C. Jama, *Mater. Chem. Phys.*, 127 (2011) 329–334.
33. F.Z. Bouanis, F. Bentiss, M. Traisnel, C. Jama, *Electrochim. Acta*, 54 (2009) 2371–2378.
34. K. Boumhara, M. Tabyaoui, C. Jama, F. Bentiss, *J. Ind. Eng. Chem.*, 29 (2015) 146–155.
35. Jingmao Zhao, G. Chen, *Electrochim. Acta*, 69 (2012) 247–255.
36. Naoual El Hamdani, Rabiaa Fdil, Mustapha Tourabi, Charafeddine Jama, F. Bentiss, *Appl. Surf. Sci.*, 357 (2015) 1294–1305.
37. M. Yadav, R.R. Sinha, S. Kumar, T.K. Sarkar, *RSC Adv*, 5 (2015) 70832–70848.
38. Ali Yousefi, Soheila Javadian, J. Neshati, *Ind. Eng. Chem. Res.*, 54 (2013) 5475–5489.
39. Sappani Hari Kumar, S. Karthikeyan, *Ind. Eng. Chem. Res.*, 52 (2013) 7457–7469.
40. Y. Qiang, S.T. Zhang, S.Y. Xu, L. Guo, N.X. Chen, I.B. Obot, *Int. J. Electrochem. Sci.*, 11 (2016) 3147–3163.
41. Ghada M. Abd El-Hafez, W.A. Badawy, *Electrochim. Acta*, 108 (2013) 860–866.
42. Yujie Qiang, Shengtao Zhang, Song Yan, Xuefeng Zou, S. Chen, *Corros. Sci.*, 126 (2017) 295–304.
43. Lei Guo, Shanhong Zhu, S. Zhang, *J. Ind. Eng. Chem.*, 24 (2015) 174–180.
44. [P. Kannan, T.S. Rao, N. Rajendran, *J. Colloid Interface Sci.* 512 (2018) 618–628.
45. Dongqin Zhang, Yongming Tang, Sijun Qi, Dawei Dong, Hui Cang, G. Lu, *Corros. Sci.*, 102 (2016) 517–522.
46. Y. Qiang, S. Zhang, Q. Xiang, B. Tan, W. Li, S. Chen, L. Guo, *RSC Adv*, 8 (2018) 38860–38871.